7

POLARIMETRIC IMAGING RADAR: ANALYSIS TOOLS AND APPLICATIONS

D. L. Evans and J. J. van Zyl

7.1 Introduction

Several existing and future Earth and planetary radars will have multipolarization capability. For example, transmit and receive polarizations can be selected independently at major planetary radar facilities such as the National Astronomy and Ionosphere Center's Arecibo Observatory in Puerto Rico and the Jet Propulsion Laboratory's Goldstone Solar System Radar in California. In addition, the S-band (2.5 GHz) Synthetic Aperture Radar (SAR) on Magellan will provide backscatter cross section estimates over most of the Venusian surface with HH polarization. During the Extended Mission, the Magellan spacecraft will be turned so that VV polarized data may also be acquired. On the terrestrial side, there are several imaging radar systems capable of acquiring multiparameter data. The Canadian Centre for Remote Sensing (CCRS) flew a multifrequency synthetic aperture radar (SAR) that operated at X-, C- and L- band from 1981–1984 and is currently upgrading the system to a digital C-band and X-band system that will acquire data at multiple polarizations (Goodenough and Livingstone, 1986). The Jet Propulsion Laboratory (JPL) developed and flew the first multipolarization SAR in which the received wave

is decomposed into two orthogonally polarized components, which independently feed two identical and coherent receiver channels, and in which reception polarization diversity is accompanied by transmission polarization diversity, so that an object's complete scattering matrix can be measured. Polarimetric radar data were acquired at L-band in Spring of 1985 using this airborne SAR. The Environmental Research Institute of Michigan (ERIM) developed an X-, C-, L-band polarimetric SAR (Kozma et al., 1986) which was completed in 1987 (see chapter by van Zyl and Zebker, in this volume for background on imaging radar polarimetry).

The Shuttle Imaging Radar (SIR-C), currently planned for flights in 1993, 1994, and 1995 will acquire multifrequency (L- and C-band), multi-incidence angle, polarimetric SAR data over the Earth's surface between 57 degrees north and south latitude, and the Earth Observing System (Eos) SAR currently planned for the late-1990's will acquire comparable data sets over the entire Earth. In 1988, the NASA/JPL Aircraft SAR was rebuilt and upgraded to a C- and L-band system so that it provides a nearly exact prototype for the C-band and L-band channels of SIR-C and the Eos SAR. In addition, a longer wavelength P-band (440 MHz) channel was added which provides a prototype to the proposed Spaceborne P-band Imaging Radar Experiment (SPIRE).

Multiparameter data sets have been acquired with the NASA/JPL Aircraft SAR over several geologic and forested areas, grasslands and sea ice. These data are being used in a variety of Earth Science investigations and to develop software tools for analysis of polarimetric data from future sensors. Examples of how recently developed tools have been used to analyze polarimetric radar images in two Earth Science investigations, a geologic process and paleoclimatology study and a forest ecology study, are described in the following sections.

7.2 Geologic Processes and Paleoclimatology

A key element in understanding the nature and significance of contemporary global change is the ability to reconstruct past climatic variables. This requires that surface processes related to past climatic conditions be identified and correlated over large regions, a task for which remote sensing is ideally suited. Key to deriving process signatures related to past climates is the development of physically based

models of the relationship between the geophysical quantities being measured and geologic information.

Weathering and depositional processes in deserts generally cause surfaces to smooth with age while erosional processes cause a roughening. The scales of these processes are different and their rates vary with climate, rock type, and geologic structure, however their effects can be used to relatively date surfaces for studies of climate change and tectonic history. Recent work has shown that relative ages of piedmont surfaces can be mapped on the basis of surface roughness changes brought about by physical weathering and aeolian deposition (e.g., Farr and Gillespie, 1984). In some cases, numerical ages have allowed preliminary derivations of the rates over time of some of these processes. For example, radiometric dates of lava flows at the Cima Volcanic Field, located approximately 120 km southwest of Las Vegas, Nevada in the Mojave Desert of California have allowed the rate of aeolian deposition on the flows to be derived (Farr and Anderson, 1987). This region is composed of some 40 cinder cones and 60 associated basaltic lava flows that range in age from 8 million years (m.y.) to 16,000 years (Dohrenwend et al., 1984; Dorn, 1984; Turrin et al., 1984). Local relief on these flows ranges up to 5 m on younger flows but is less than 1 m on flows older than 0.25 m.y.

The geomorphic evolution of the Cima flows has been described by Wells et al. (1985). Systematic changes in the flow surfaces were found to be caused by cyclic changes in the rates of aeolian deposition, soil formation, and fluvial erosion. These cycles were interpreted to be the result of changes in climate alternating between warmer, dryer interglacial and cooler, wetter glacial periods. Wells et al. (1985) made morphologic measurements on flows of different age in order to quantify the changes they observed. One of the most prominent and consistent changes observed and measured was the change in surface relief or roughness with time. This is caused mainly by rubbling of flow projections and by filling in of flow depressions with wind-blown silt.

Changes in surface roughness with age in the Cima area were analyzed using L-band polarization signatures of the different units by Evans et al. (1988). The concept of the polarization signature of a scatterer was used by van Zyl et al. (1987) and Zebker et al. (1987) to plot the power of a return wave as a function of transmit and receive polarizations. In addition to the co- and cross-polarized polarization signatures for which both transmit and receive polarizations are specified,

Evans et al. (1988) introduced polarized and unpolarized signatures which depict the relative power of the return wave for all transmit polarizations. These signatures taken together represent a more complete description of the polarimetric scattering properties of a surface. Evans et al. (1988) noted that the unpolarized return was the most sensitive to the effects of age on lava flow surfaces and concluded that trends in the unpolarized signatures were consistent with a decrease in "pedestal height" (see van Zyl and Zebker, this volume) caused by decreasing roughness with age.

As described in Evans et al. (1988), knowledge of the Stokes vector of the received signal allows the decomposition of a partially polarized signal into completely polarized and completely unpolarized components, where the partially polarized signal may be regarded as the sum (e.g., Kraus, 1966):

$$\begin{pmatrix} S_0 \\ S_1 \\ S_2 \\ S_3 \end{pmatrix} = S_0 \begin{pmatrix} 1-d \\ 0 \\ 0 \\ 0 \end{pmatrix} + S_0 \begin{pmatrix} d \\ d\cos(2\chi)\cos(2\psi) \\ d\cos(2\chi)\sin(2\psi) \\ d\sin(2\chi) \end{pmatrix}$$

where

$$\begin{pmatrix} S_0 \\ S_1 \\ S_2 \\ S_3 \end{pmatrix} = \begin{matrix} \text{Stokes vector of average} \\ \text{received signal from a region} \end{matrix}$$

$$d = \frac{\sqrt{S_0^2 + S_1^2 + S_3^2}}{S_0}$$

χ = wave ellipticity angle

ψ = wave orientation angle

$$\begin{pmatrix} d \\ d\cos(2\chi)\cos(2\psi) \\ d\cos(2\chi)\sin(2\psi) \\ d\sin(2\chi) \end{pmatrix} = \begin{matrix} \text{Stokes vector of completely polarized part} \\ \text{of the average received signal from a region} \end{matrix}$$

Figure 7.1 is a total power L-band image of the Cima Volcanic Field showing areas where unpolarized signatures have been extracted from lava flow units with three different ages. Figure 7.2 shows the C-, L- and P-band unpolarized signatures from these three units. Unit i_1 is dated at 0.14 million years (m.y.), Unit r_2 at 0.7 m.y., and Unit

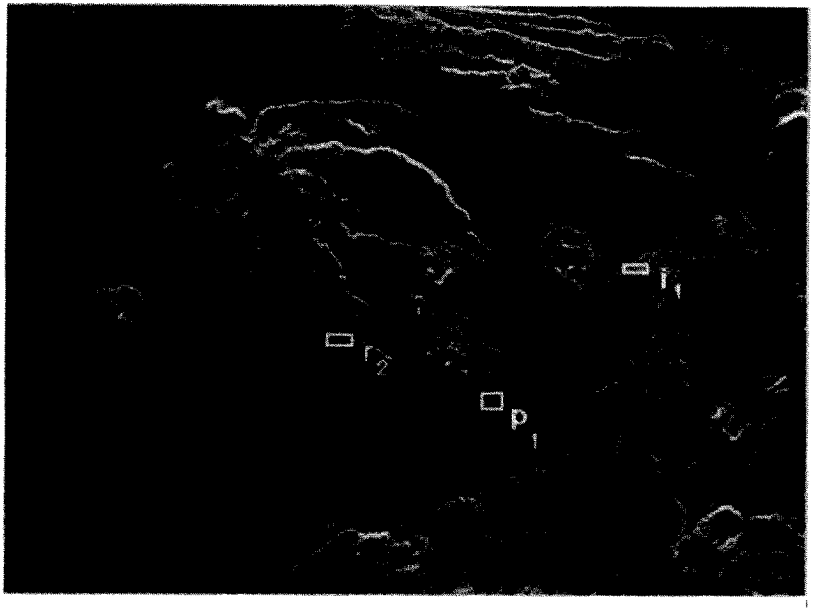

Figure 7.1 Total power L-band image of the Cima Volcanic Field showing areas where unpolarized signatures have been extracted from lava flow units with three different ages.

p_1 at 0.6-1.1 m.y. (Dohrenwend et al., 1984). Figure 7.2 shows that L-band unpolarized signatures decrease with age as noted in Evans et al. (1988). However, while the unpolarized C-band return decreases from Unit i_1 to Unit r_2, it increases from Unit r_2 to Unit p_1. In the P-band case, there is a continued increase in unpolarized return going from the youngest to the oldest units.

These trends can be explained by investigating the Wells et al. (1985) model in more detail. As mentioned, Wells et al. (1985) observed consistent changes in roughness with time caused mainly by rubbling of flow projections and by filling in of flow depressions with wind-blown silt. However, after approximately 1 m.y., drainages develop causing an apparent roughening of the surface. Models of these

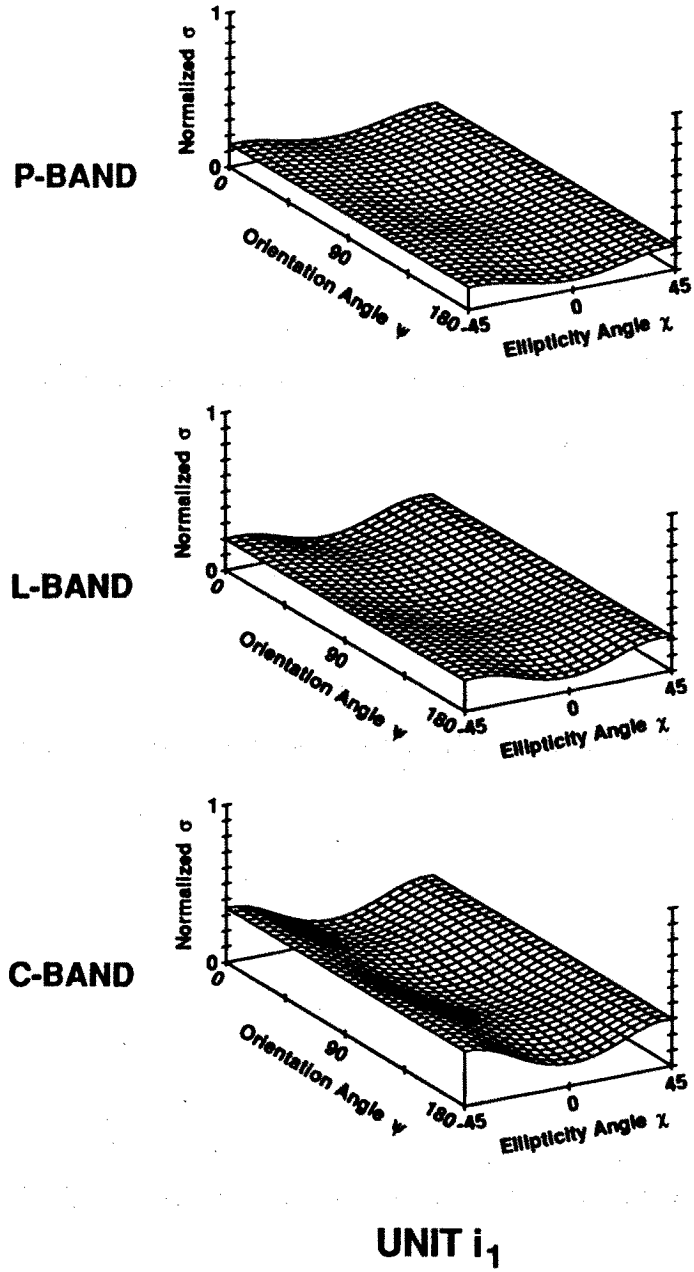

Figure 7.2a C-, L- and P-band unpolarized signatures from Unit i_1 (dated at 0.14 million years).

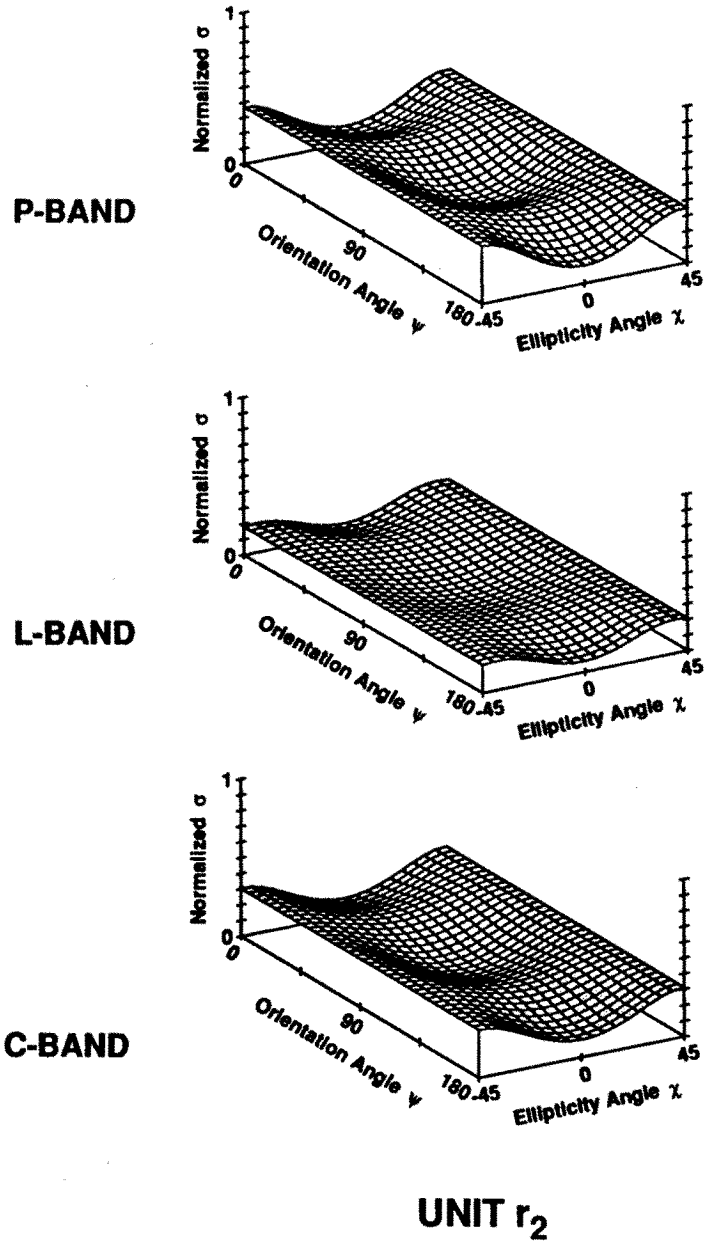

Figure 7.2b C-, L- and P-band unpolarized signatures from Unit r_2 (dated at 0.7 million years).

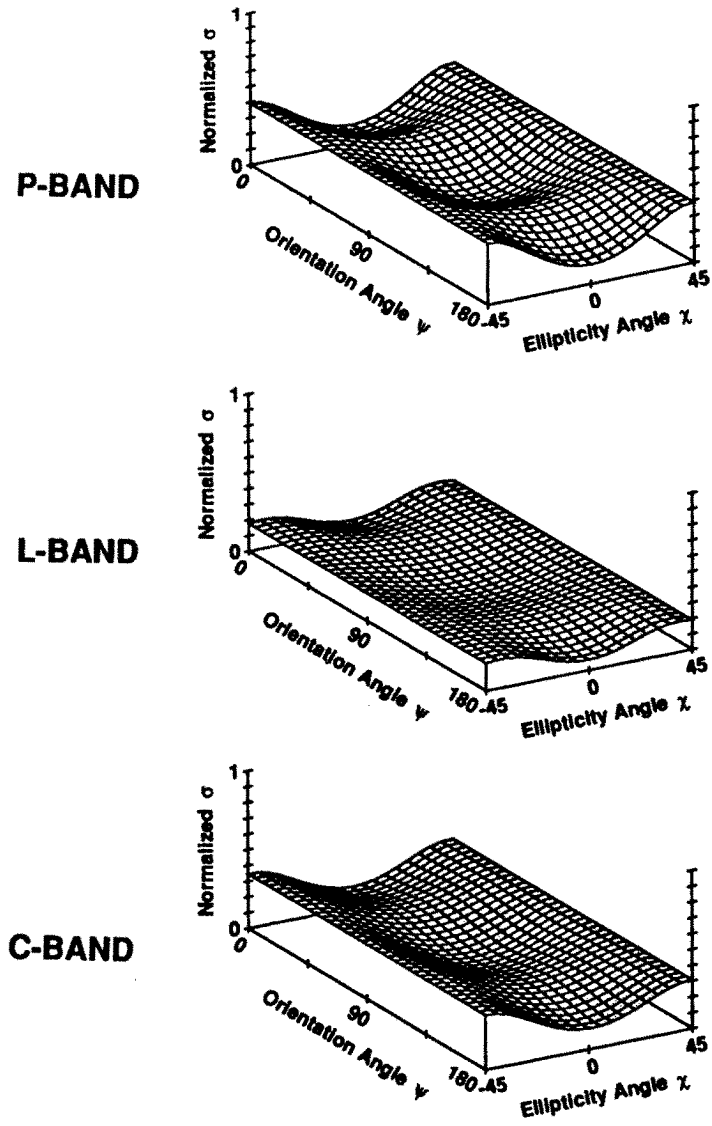

Figure 7.2c C-, L- and P-band unpolarized signatures from Unit p_1 (0.6-1.1 m.y.). Note that L-band unpolarized signatures decrease with age. However, while the unpolarized C-band return decreases from i_1 to Unit r_2, it increases from Unit r_2 to Unit p_1. In the P-band case, there is a continued increase in unpolarized return going from the youngest to the oldest units.

three representative stages of landscape evolution are shown diagrammatically in Fig. 7.3. The signatures in Fig. 7.2 are consistent with an overall smoothing from about 0.1 to 0.2-0.7 m.y. at roughness scales where L- and C-band are sensitive, then an increase in roughness at C-band scales caused by rougher surfaces being exposed as drainages develop. It appears that the P-band may be penetrating the windblown silt that fills in flow depressions, resulting in increased multiple scattering with age.

The results presented here indicate that multifrequency polarization signatures provide a link between geologic processes and radar remote sensing data. Future work will emphasize the quantitative determination of the physical state of the surface which should allow direct comparison between different areas in terms of the absolute roughness of surfaces and the rate of modification under different conditions. Specifically, radar backscatter models and inversion techniques are being developed that will allow backscatter data acquired at multiple angles, frequencies, and polarizations to be inverted to yield estimates of dielectric constant and surface roughness at scales from approximately 2 cm to 1 m. These estimates can then be used as measures of the amount and type of physical modification of a surface. Once the spatial distribution of these modification processes can be determined, it will be possible to relatively date surfaces for studies of climate change and tectonic history.

7.3 Forest Ecology

Another key element in understanding global change is the ability to quantify sources and sinks of greenhouse gases such as CO_2, CH_4, and N_2O. For example, the magnitude of the carbon source and sink strength in forests depends largely on the successional stage. In addition, forests are being rapidly cleared for agriculture and pasture resulting in a relatively instantaneous (depending on whether the forest in burned or left to decompose) influx of CO_2 in the atmosphere. Information on (1) the biomass of the existing forests, (2) the areal extent of the cleared forests, and (3) the successional stage of primary and secondary growth forests (and thus the carbon source/sink strength) are all essential to understanding the role of forests in the global carbon cycle.

Several studies have shown that radar may be an effective tool for analysis of deforestation and reforestation, and possibly determination

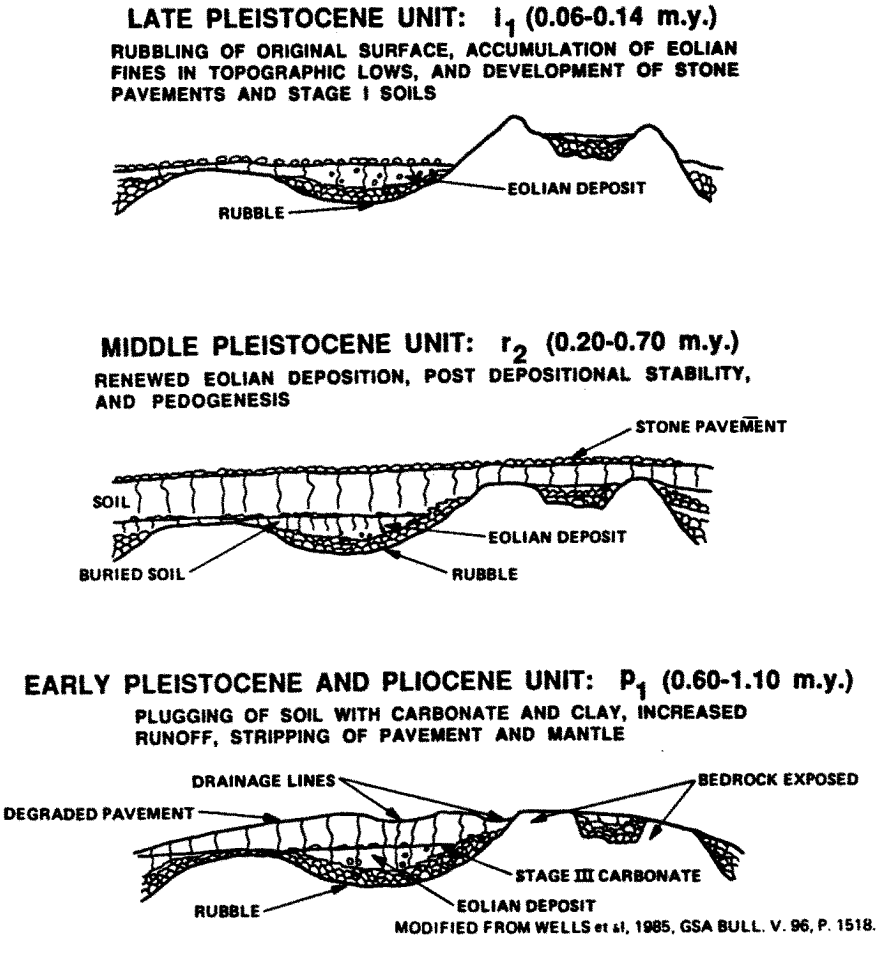

Figure 7.3 Models of these three representative stages of landscape evolution (modified from Wells et al., 1985).

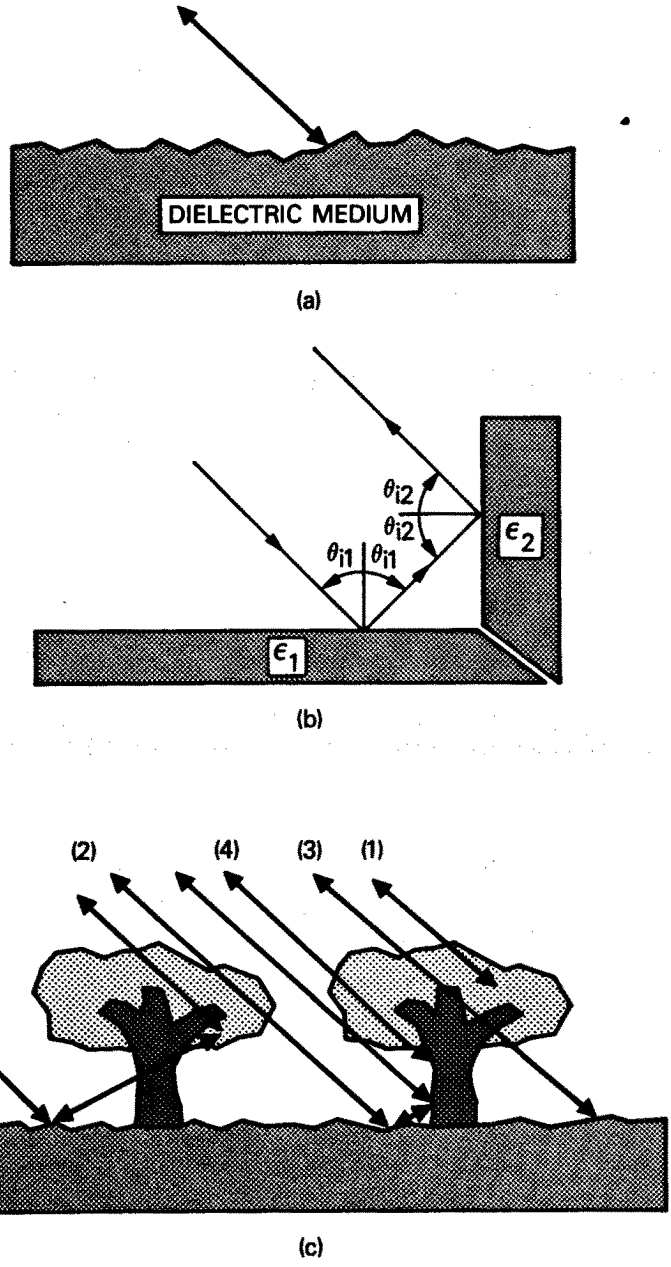

Figure 7.4 Geometry for a) single (odd) reflection, b) double (even) reflection, c) diffuse reflection. (1) represents direct backscatter from the canopy, (2) represents signals that were scattered twice, (3) represents direct backscatter from the ground surface, and (4) represents direct backscatter from the tree trunks.

of above-ground woody biomass and successional stage (Hoffer et al., 1986; Richards et al., 1987; Paris and Kwong, 1988; Sun and Simonett, 1988 a,b). van Zyl (1989) described an unsupervised classification technique which is useful for interpreting scattering from forested areas and was used in Evans et al. (1988) to map clear cut areas that were not discernable in L-band HH and VV images.

The unsupervised algorithm described in van Zyl (1989) classifies scatterers into one of three types based on the relationship between the orientation angles and handedness of the transmit polarization to the corresponding parameters of the receive wave for each transmit polarization. The first class of scattering is single reflection. Using Rice's (1951) rough-surface scattering model as extended by Peake (1959) and Valenzuela (1967), one would expect that in the case of a slightly rough dielectric surface the incident wave would experience little multiple scatter (Fig. 7.4a). In this case, HH and VV signals are in phase, and the orientation angle of the scattered wave increases as the orientation angle of the transmitted wave increases, and decreases as the orientation angle of the transmitted wave decreases. The handedness of the scattered wave, however, would be the opposite of that of the transmitted wave polarization. That is, for example, a left-hand elliptically polarized wave would be returned as a right-hand elliptically polarized wave.

The second class of scattering (Fig. 7.4b) is from a dihedral corner reflector, and exhibits a double-bounce geometry, resulting in a 180 degree phase shift between HH and VV. In this case, the orientation angle of the scattered wave decreases as the orientation angle of the transmitted wave increases. The handedness of the scattered wave polarization is the same as that of the transmitted wave polarization so that the ellipticity angles for the transmitted and scattered waves have the same sign.

For the third class of scattering, a diffusely scattering area exhibiting multiple interactions, a different behavior occurs. Due to the multiple interactions, the highly varying HH to VV phase difference over the area exhibits a noise-like character. The resulting Stokes matrix elements imply that the orientation angle of the average scattered wave tracks that of the transmitted wave, a behavior similar to that observed for the single-bounce case. However, the handedness of the scattered wave is the same as that of the transmitted wave polarization which is more consistent with a double-bounce mechanism. Evans et

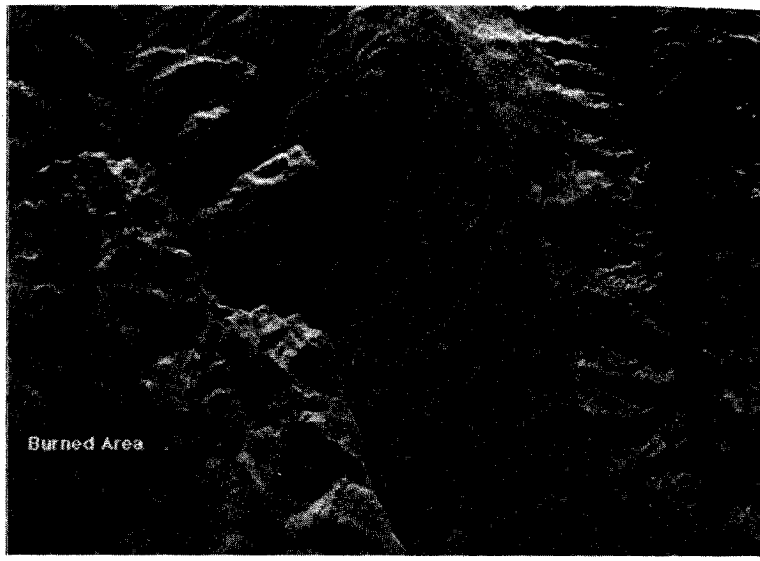

Figure 7.5 Total power L-band image of an area near Mt. Shasta, CA.

al. (1988), and van Zyl (1989) noted that this behavior is generated by a class of "three-layer" vegetation models such as the one shown in Fig. 7.4c and described in van Zyl (1985), Richards et al. (1987), Ulaby et al. (1988) and Durden et al. (1989).

As discussed in van Zyl (1989), in a three-layer forest model consisting of a slightly rough ground surface at the bottom, a layer of randomly oriented dielectric cylinders oriented statistically around the vertical direction that represents the tree trunks, and a layer of randomly oriented dielectric cylinders that represents the major limbs of the trees, one expects a number of scattering processes to be important. The most important ones at L-band are: 1) direct backscatter from the top layer of the canopy (single reflection), 2) double reflections from the ground surface to the tree trunk or limbs (two forward reflections), 3) direct backscatter from the ground (single reflection), and 4) direct backscatter from the tree trunks (single reflection). By varying the number of cylinders in the two vegetation layers, van Zyl (1989) observed that for very sparse canopies, direct backscatter from the ground dominates and the area is classified as dominated by an odd

number of reflections. In somewhat thicker canopies, scattering is dominated by the ground/trunk double reflections, and the area is classified as being dominated by an even number of reflections. If the canopy density is further increased, direct backscatter from the branches and ground/trunk double reflections become comparable, and the area exhibits the characteristics described for the diffuse class. Finally, for very thick canopies, where direct backscatter from the branches dominates, the area is classified as being dominated by odd reflections. The exact points at which these transition from one class to the other are functions of radar frequency, forest density and trunk water content (cylinder dielectric constant).

Figure 7.5 shows an L-band total power image of an area in Mt. Shasta in northern California. This area contains conifers and some hardwoods (Durden et al., 1989). According to Durden et al. (1989), the area at the lower left of this image is a burned area with somewhat smaller trees (35 meters versus 45 meters for the unburned trees). Figure 7.6 shows classification results based on C-, L-, and P-band data of the same area. One can see in Fig. 7.6a that much of the area is classified as dominated by single reflections at C-band, indicating that the canopy is dense enough to result in single reflections from the branches, and the clear cut areas allow single reflections from the ground surface. At L-band, while the clear cut areas are still dominated by single reflections, there is a much more pervasive diffuse scattering by the canopy, in both the burned and unburned areas, and some double reflection. At P-band, the clear cuts are more visible and the burned area in the lower left of the image exhibits significantly more scattering caused by double reflections. This increase could either be caused by the difference in the size of the trees as noted above or some change in the canopy as a result of the fire that results in increased penetration into the burned area. According to Durden et al. (1989), there is also a decrease in the P-band unpolarized signature of the burned area relative to the unburned area. They conclude based on model results that this may be caused by a lower dielectric constant in the burned area, which would explain the increased canopy penetration seen here.

The results presented here indicate that multifrequency polarimetric radar data provides the ability to isolate the scattering pathway which interacts mostly with tree trunks and stems, which is key to extracting biophysical parameters such as woody biomass (i.e., height and diameter of tree trunks and stems) and possibly trunk water con-

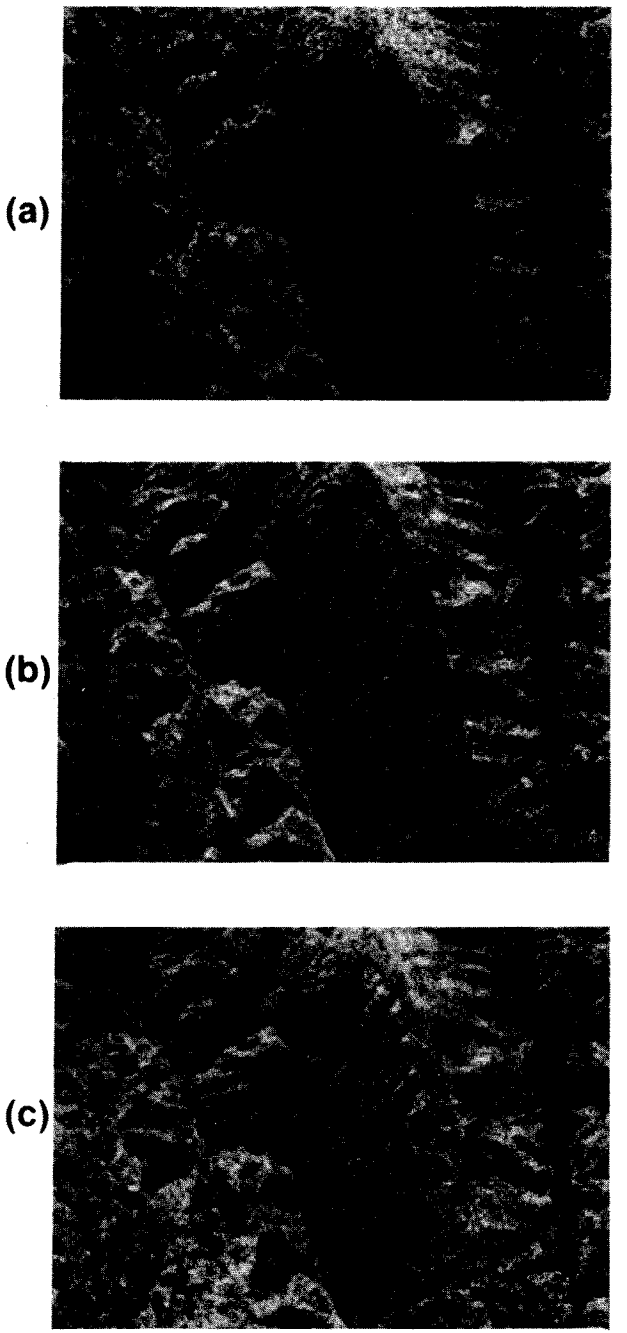

Figure 7.6 Classification results based on a) C-, b) L-, and c) P-band data of the Shasta area. Pixels classified in red are consistent with a double reflection, in blue, with a single reflection and in green with a diffuse reflection [see color plate 7.1 (a), (b), and (c)].

tent. Thus, as in the case of geological process studies, future work will emphasize the development of radar backscatter models and model inversion algorithms which can be used to convert radar parameters to biogeophysical parameters directly.

7.4 Summary

In this chapter, we give examples of recently developed software tools that enable scientists to analyze polarization signatures of natural targets and to identify probable scattering mechanisms for each pixel in a radar image, and discuss how these tools have been used to analyze radar images for two Earth Science investigations. The results presented here for a geologic process and paleoclimatology example indicate that multifrequency polarization signatures provide a link between geologic processes related to past climatic conditions and radar remote sensing data. The results of a forest ecology example indicate that multifrequency polarimetric radar data provide the ability to isolate the scattering pathway which interacts mostly with tree trunks and stems, which is key to extracting biophysical parameters such as woody biomass (i.e., height and diameter of tree trunks and stems) and possibly trunk water content. Derivation of process-related information and biogeophysical parameters from remote sensing data is key to our understanding the nature and significance of contemporary global change. Thus, future work will emphasize the quantitative determination of the physical state of the Earth's surface and cover through the development of radar backscatter models and model inversion algorithms which can be used to convert radar parameters to biogeophysical parameters directly.

Acknowledgments

This work was performed at the Jet Propulsion Laboratory, California Institute of Technology, sponsored by the National Aeronautics and Space Administration. We would like to thank the people in the Radar Science and Engineering Section at JPL who operated the imaging polarimeter and processed the data used in this manuscript.

References

[1] Dohrenwend, J. C., L. D. McFadden, B. D. Turrin, and S. G. Wells, "K-Ar dating of the Cima Volcanic Field, Eastern Mojave Desert, California: Late Cenozoic volcanic history and landscape evolution," *Geology*, **12**, 163–167, 1984.

[2] Dorn, R. I., "Geomorphological interpretation of rock varnish in the Mojave Desert," California, in Dohrenwend, J. C., ed., Surficial Geology of the Eastern Mojave Desert, California, Guidebook, *Geol. Soc. Amer.*, Ann. Meeting, Reno, NV, 1984.

[3] Durden, S. L., J. J. van Zyl, and H. A. Zebker, "Modeling and observation of forest radar polarization signatures," *IEEE Trans. on Geoscience and Remote Sensing*, **27**, No. 3, 290–30, 1988.

[4] Evans, D. L., T. G. Farr, J. J. van Zyl, and H. A. Zebker, "Radar polarimetry: Analysis tools and applications," *IEEE Trans. Geoscience and Remote Sensing*, **26**, No. 6, 774–789, 1988.

[5] Farr, T. G., and R. S. Anderson, "Simulation of surface modification processes in arid regions: Applications to remote sensing and the study of climate change," *Geol. Soc. Amer., Abs. with Prog.*, **19**, 659, 1987.

[6] Farr, T. G., and A. R. Gillespie, "Measurement of micro-relief on alluvial fans and its relation to age, lithology, and radar response," *Geol. Soc. Amer., Abs. with Prog.*, **16**, 506, 1984.

[7] Goodenough, D. G., and C. Livingstone, *IGARSS 1985 Digest*, 686, 1986.

[8] Hoffer, R. M., D. F. Lozano-Garcia, A. R. Gillespie, P. W. Mueller, and M. J. Ruzek, "Analysis of multiple incidence angle SIR-B data for determining forest stand characteristics," *The Second Spaceborne Imaging Radar Symposium*, JPL Publication 86-26, 159–164, 1986.

[9] Kozma, A., A. D. Nichols, R. F. Rawson, S. J. Shackman, C. W. Haney and J. J. Shanne, " Multifrequency-polarimetric SAR for Remote Sensing," *Proc. of IGARSS'86 Symposium*, **ESA SP–254**, 715–720, 1986.

[10] Kraus, J. D. Radio Astronomy, McGraw Hill, 486 p., 1966.

[11] Paris, J. T., and H. Kwong, "Characterization of vegetation with combined Thematic Mapper (TM) and Shuttle Imaging Radar (SIR-B) image data," Photogrammetric Engineering and Remote Sensing, **54**, 1187–1193, 1988.

[12] Peake, W. H., "Theory of Radar Return from Terrain," *IRE National Conv. Rcc. 7*, **Part 1**, 27–41, 1959.

[13] Rice, S. O., "Reflection of electromagnetic waves from slightly rough surfaces," *Comm. Pure Appl. Math*, **4**, 351–378, 1951.

[14] Richards, J. A., G. Sun and D. Simonett, "L-band radar backscatter modeling of forest stands," *IEEE Trans. on Geoscience and Remote Sensing*, **25**, 487–498, 1987.

[15] Sun, G. Q., and D. S. Simonett, "Simulation of L-band HH radar backscattering from coniferous forests stands: A comparison with SIR-B Data," *International Journal of Remote Sensing*, **9**, 907–925, 1988(a).

[16] Sun, G. Q., and D. S. Simonett, "A composite L-band radar backscattering model for coniferous forest stands," *Photogrammetric Engineering and Remote Sensing*, **54**, 1195–1201, 1988(b).

[17] Turrin, B. D., J. C. Dohrenwend, S. G. Wells, and L. D. McFadden, "Geochronology and eruptive history of the Cima volcanic field," Eastern Mojave Desert, California, Guidebook, *Geol. Soc. Amer.*, Ann. Meeting, Reno, NV, 1984.

[18] Ulaby, F. T., K. Sarabandi, K. McDonald, M. Whitt, M. C. Dobson, *Michigan Microwave Canopy Scattering Model (MIMICS)*, University of Michigan Radiation Laboratory Publication **022486-T-1**, 188 pgs, 1988.

[19] Valenzuela, G. R. "Depolarization of EM waves by slightly rough surfaces," *IEEE Trans. on Ant. and Prop.*, **AP-15**, 552–557, 1967.

[20] van Zyl, J. J. "On the importance of polarization in radar scattering problems," *Ph. D. Thesis,* Caltech Antenna Lab Report no. 120, 32–33, 1985.

[21] van Zyl, J. J., H. A. Zebker and C. Elachi, "Imaging radar polarization signatures: Theory and observation," *Radio Science,* **22**, no. 4, 529–543, 1987.

[22] van Zyl, J. J., "Unsupervised classification of scattering behav-

ior using radar polarimetry data," *IEEE Trans. Geoscience and Remote Sensing,* **27**, no. 1, 36–45, 1989.

[23] Wells, S. G., J. C. Dohrenwend, L. D. McFadden, B. D. Turrin, and K. D. Mahrer, "Late Cenozoic landscape evolution on lava flow surfaces of the Cima volcanic field," Mojave Desert, California, *Geol. Soc. Amer.* Bull., **96**, 1518–1529, 1985.

[24] Zebker, H. A., J. J. van Zyl and D. N. Held, "Imaging radar polarimetry from wave synthesis," *Jour. Geophys. Research,* **92**, no. B1, 683–701, 1987.